NANO LETTERS
Letter
Cite This: Nano Lett. 2019, 19, 8572−8580
pubs.acs.org/NanoLett

Observation of the Kondo Effect in Multilayer Single-Crystalline VTe_2 Nanoplates

Hongtao Liu,[†,#] Yunzhou Xue,[‡,#] Jin-An Shi,[§] Roger A. Guzman,[§] Panpan Zhang,[†] Zhang Zhou,[†] Yangu He,[†,⊥] Ce Bian,[†] Liangmei Wu,[†] Ruisong Ma,[†] Jiancui Chen,[†] Jiahao Yan,[†] Haitao Yang,[†] Cheng-Min Shen,[†,∥] Wu Zhou,[§] Lihong Bao,*[,†,∥] and Hong-Jun Gao[†]

[†]Institute of Physics & University of Chinese Academy of Sciences, Chinese Academy of Sciences, Beijing 100190, P.R. China
[‡]College of Chemistry and Environmental Engineering, Shenzhen University, Shenzhen 518060, P.R. China
[§]School of Physical Sciences and CAS Key Laboratory of Vacuum Physics, University of Chinese Academy of Sciences, Beijing 100049, China
[∥]Songshan Lake Materials Laboratory, Dongguan, Guangdong 523808, P.R. China
[⊥]Department of Physics, Applied Physics, and Astronomy, Rensselaer Polytechnic Institute, 110 Eighth Street, Troy, New York 12180, United States

Supporting Information

ABSTRACT: We report the chemical vapor deposition (CVD) growth, characterization, and low-temperature magnetotransport of 1T phase multilayer single-crystalline VTe_2 nanoplates. The transport studies reveal that no sign of intrinsic long-range ferromagnetism but localized magnetic moments exist in the individual multilayer metallic VTe_2 nanoplates. The localized moments give rise to the Kondo effect, evidenced by logarithmical increment of resistivity with decreasing temperature and negative magnetoresistance (NMR) regardless of the direction of magnetic field at temperatures below the resistivity minimum. The low-temperature resistivity upturn is well described by the Hamann equation, and the NMR at different temperatures, a manifestation of the magnetization of the localized spins, is well fitted to a Brillouin function for $S = 1/2$. Density functional theory calculations reveal that the localized magnetic moments mainly come from the interstitial vanadium ions in the VTe_2 nanoplates. Our results will shed light on the study of magnetic properties, strong correlation, and many-body physics in two-dimensional metallic transition metal dichalcogenides.

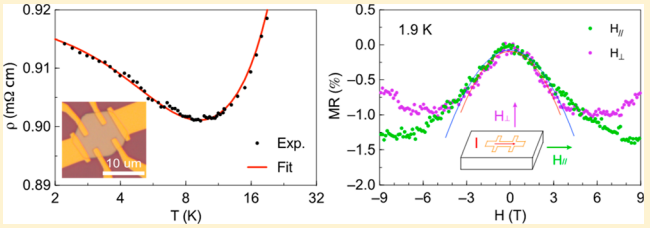

KEYWORDS: *VTe_2, chemical vapor deposition, low-temperature transport, Kondo effect, DFT calculations*

Recent discovery of intrinsic ferromagnetism in few-layer two-dimensional (2D) van der Waals crystals, such as CrI_3 and $Cr_2Ge_2Te_6$,[1,2] has inspired active research in enriching the library of 2D magnetic materials.[3−5] Theoretical calculations have predicted that monolayer vanadium-based transition metal dichalcogenides (TMD) with chemical formula of VX_2 (X = S, Se, Te) are intrinsically ferromagnetic.[6−10] Strong room-temperature ferromagnetism has been observed in monolayer VSe_2 grown on HOPG and MoS_2 by molecular beam epitaxy.[11] However, the ferromagnetic order in VSe_2 diminishes rapidly as the layer number increases, and bulk VSe_2 is considered paramagnetic. Magnetic properties in bulk VSe_2 are attributed to the interstitial vanadium ions.[12−15] The interstitial vanadium ions provide local magnetic moments due to localized 3d electrons, and the localized magnetic moments induced Kondo effect in bulk VSe_2 has been observed.[16] A lattice of interstitial vanadium ions in V_5S_8 (or $V_{0.25}VS_2$) gives rise to antiferromagnetic ordering in bulk and weak ferromagnetism in ultrathin V_5S_8 flakes.[17,18] However, whether the local magnetic moments will be formed by interstitial vanadium ions in VTe_2 remains elusive.[19]

Dilute magnetic impurities in a metal will lead to the Kondo effect.[20] The Kondo effect is a many-body interaction between conduction electrons of nonmagnetic host and local moment of individual magnetic impurity through s-d exchange interaction, which leads to a resistivity minimum well described by $\Delta\rho = -c \ln T$, where T is the temperature and c is a parameter depending on the host metal and the species and concentration of magnetic impurities.[20,21] This expression is only valid for temperatures well above the characteristic Kondo temperature T_K, as the Ruderman−Kittel−Kasuya−Yosida (RKKY) interaction between the dilute magnetic impurities through the conduction electrons can be neglected at the temperature around and above T_K.[20] The impurities are

Received: July 29, 2019
Revised: October 26, 2019
Published: November 8, 2019

DOI: 10.1021/acs.nanolett.9b03100
Nano Lett. 2019, 19, 8572−8580

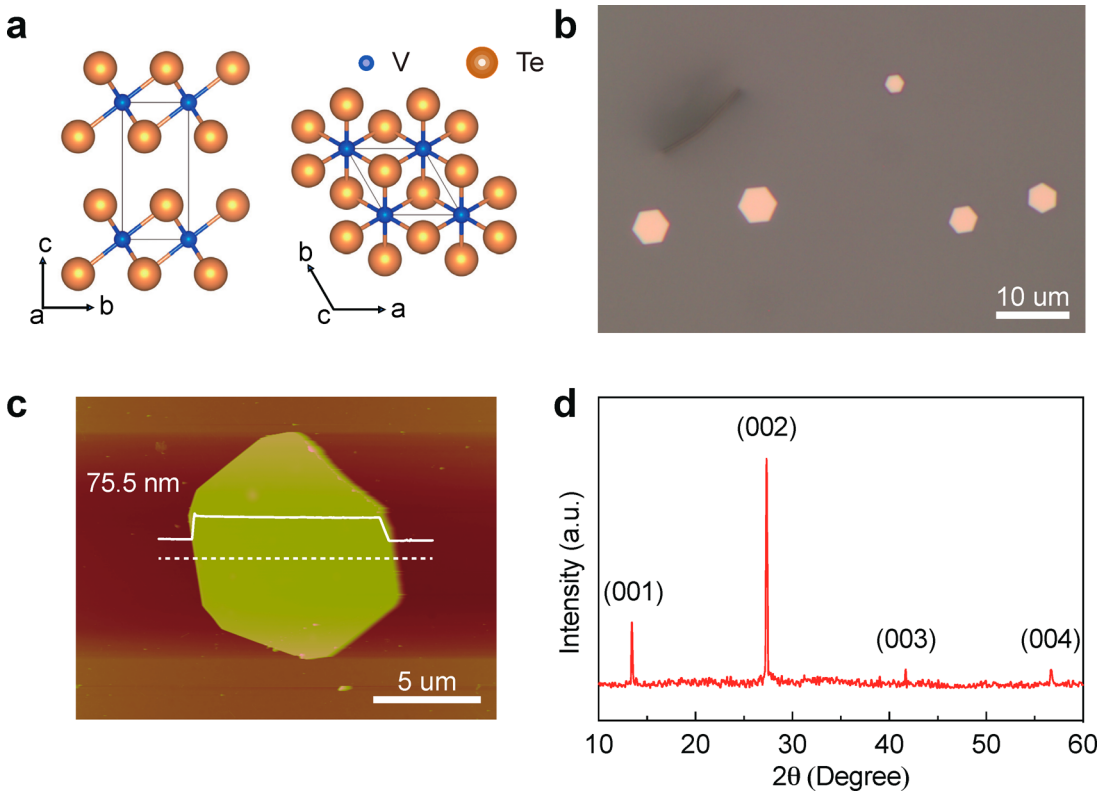

Figure 1. VTe_2 nanoplates grown by a sublimed-salt-assisted atmospheric pressure CVD method. (a) Atomic model of 1T phase VTe_2. (b) Optical image of the hexagonal-shape VTe_2 nanoplates grown on mica. The black line is a vertical standing VTe_2 nanoplate. (c) AFM image and height profile of a VTe_2 nanoplate with a thickness of 75.5 nm. (d) Room-temperature XRD pattern of the VTe_2 nanoplates.

paramagnetic at the temperature above T_K. However, for $T \ll T_K$ the spin of magnetic impurities will be compensated forming a many-body singlet ground state, the Kondo singlet. Resistivity saturates toward $T \rightarrow 0$ K due to the nonmagnetic scattering of the Kondo singlet. Dilute magnetic impurities are typically introduced by defects or magnetic dopants.[22−27] As mentioned above, the unpaired d-electron of vanadium ions, particularly the interstitial vanadium ions, in VX_2 can give rise to localized moments or even magnetic ordering. Predictably, a trace amount of interstitial vanadium ions in VX_2 will lead to the Kondo effect.[16,19] Quite recently single-crystalline VTe_2 nanoplates with thickness ranging from ∼90 to 8 nm have been grown by chemical vapor deposition (CVD) and room-temperature ferromagnetism is observed.[28] However, the magnetic properties are obtained in samples of VTe_2 nanoplates with various thicknesses and sizes. Magnetic properties of individual VTe_2 nanoplates, particularly studied by transport, and the origin of magnetic moments remain elusive.

Here, we report the preparation, characterization, and low-temperature magnetotransport of high-quality single-crystalline 1T phase multilayer VTe_2 nanoplates. The VTe_2 nanoplates are grown by a sublimed-salt-assisted atmospheric pressure CVD method and characterized by optical microscope (OM), atomic force microscopy (AFM), X-ray diffraction (XRD), X-ray photoelectron spectroscopy (XPS), scanning electron microscopy (SEM), and transmission electron microscopy (TEM). Low-temperature transport studies demonstrate that all the multilayer VTe_2 nanoplates are metallic and no signature of long-range ferromagnetic order exists. Instead, localized magnetic moments are presented in the individual multilayer VTe_2 nanoplates, which lead to the Kondo effect. The Kondo effect is manifested by low-temperature upturn in resistivity and negative magnetoresistance (NMR) independent of the direction of magnetic field. Scattering of conduction electrons by the localized magnetic moments through isotropic s-d exchange interaction leads to the resistivity minimum and NMR at low magnetic fields, both of which are analyzed within the framework of the Kondo model. Density functional theory (DFT) calculations demonstrate that interstitial vanadium ions in VTe_2 provide the localized moments.

1T phase multilayer VTe_2 nanoplates were synthesized by a sublimed-salt-assisted atmospheric pressure CVD method.[29] Tellurium lump and finely ground V_2O_5/NH_4Cl (1:20, wt) powder were used as the tellurium source and vanadium source, respectively. VTe_2 nanoplates were grown at the temperature of 750 °C in 20 min followed by rapid cooling down to room temperature with 300 sccm hydrogen/argon (1:9, v/v) as carrier gas in the whole process. Before growth, the furnace was first evacuated by a rotary pump to remove any residual air in the system and then filled with the carrier gas to atmospheric pressure. The evacuation process is of vital importance to the growth of VTe_2 nanoplates. No VTe_2 nanoplates or VTe_2 nanoplates with poor quality will grow without the pre-evacuation process. Some VTe_2 nanoplates grow vertically on the substrate, which makes the transfer of VTe_2 nanoplates to other substrates much easier without any contamination.

Figure 1a shows the atomic structure of 1T phase VTe_2. It crystallized in a trigonal layered structure in the space group $P\bar{3}m1$ (164) with lattice constants of $a = b = 3.636$ Å and $c = 6.51$ Å.[28] Each monolayer is composed of a layer of

DOI: 10.1021/acs.nanolett.9b03100
Nano Lett. 2019, 19, 8572−8580

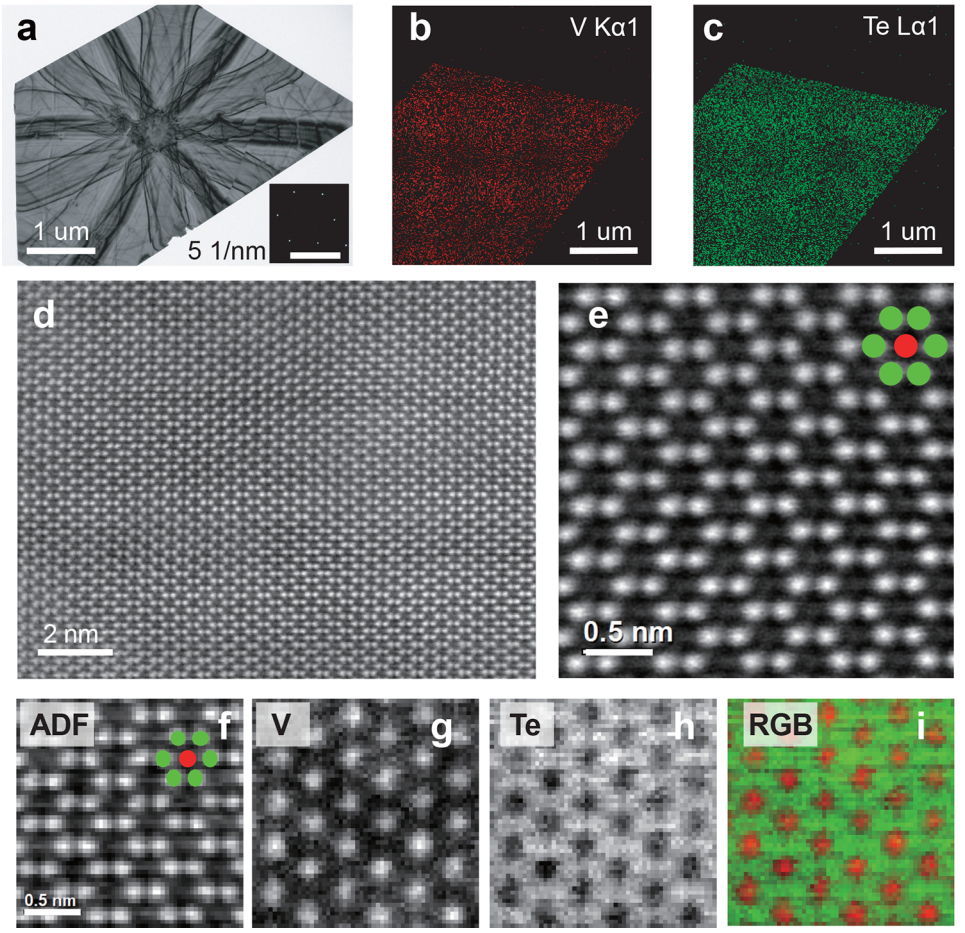

Figure 2. TEM characterization of the single crystallinity of the as-grown 1T phase VTe_2 nanoplates. (a) Low-magnification TEM image of a VTe_2 nanoplate and the corresponding EDS elemental mapping images of (b) vanadium (V) and (c) tellurium (Te) for the upper right corner of the nanoplate in (a). Inset in (a) is the SAED pattern of the nanoplate. (d) Low-magnification and (e) close-up HAADF-STEM images of the VTe_2 nanoplate viewed along the ⟨001⟩ zone axis. The Te atoms are the brighter columns, whereas the V columns show weak contrast. Green and red dots correspond to Te and V, respectively. (f) HAADF-STEM image acquired simultaneously during EELS mapping. EELS mapping of the (g) V $L_{2,3}$ edge, (h) Te $M_{4,5}$ edge, and (i) RGB colored map enhancing the contrast of the V and Te maps. V is red and Te is green.

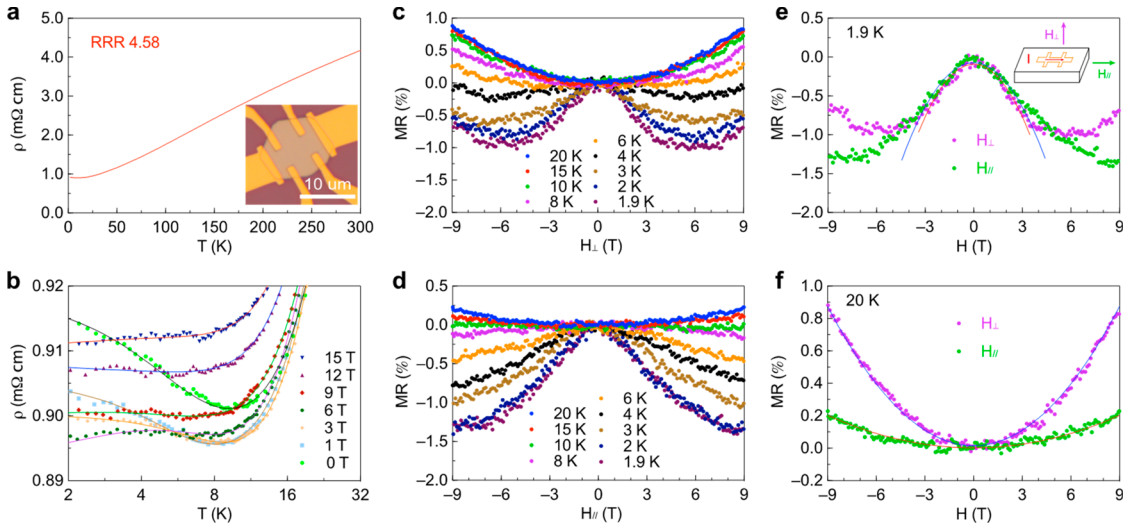

Figure 3. Low-temperature transport properties of the multilayer VTe_2 nanoplates. (a) Temperature-dependent resistivity ($\rho-T$) for the device with optical image showed in the inset. (b) Logarithmic low-temperature-dependent resistivity under different magnetic fields. Solid lines are fits to the Kondo model. Relative magnetoresistance (MR) at different temperatures with the magnetic field (c) perpendicular (transverse MR) and (d) parallel (longitudinal MR) to the plane of the sample, respectively. (e,f) Transverse and longitudinal MR with low magnetic field fits (solid lines) to expression MR (%) = $aH^2 + b$ at 1.9 and 20 K respectively.

DOI: 10.1021/acs.nanolett.9b03100
Nano Lett. 2019, 19, 8572−8580

hexagonally arranged vanadium ions, sandwiched between two layers of tellurium ions in octahedral coordination. The layers are held together via weak van der Waals forces. Figure 1b shows a typical optical image of the VTe_2 nanoplates grown on mica. The as-grown multilayer VTe_2 nanoplates are usually in hexagonal or semihexagonal shape, whereas for ultrathin VTe_2 nanoplates they are usually suborbicular (Figures 1b,c and S2–S6). Room-temperature XRD pattern (Figure 1d) of the VTe_2 nanoplates with various thicknesses and shapes agrees well with that of 1T phase VTe_2,[28] suggesting that all the VTe_2 nanoplates share the same 1T phase crystalline structure. The VTe_2 nanoplates may segregate from tellurium liquid drops via a vapor–liquid–solid growth mechanism, which is shown in Figure S2b. The single-crystalline structure of the 1T phase VTe_2 is further confirmed by TEM as shown in Figure 2. Energy dispersive spectrum (EDS) mappings of vanadium and tellurium show uniform distribution of the two elements (Figure 2b,c). The atomic ratio of tellurium and vanadium is close to 2:1, as shown in Figure S4e. Selected-area electron diffractions (SAED) show clear spots and are almost the same orientation at different locations of the VTe_2 nanoplate (Figures 2a (inset) and S5), which demonstrates the single-crystalline nature of the VTe_2 nanoplate. Atomic-resolution high-angle annular dark-field scanning TEM (HAADF-STEM) images in Figures 2d,e and S7 show the perfect atomic structure of the as-grown VTe_2 nanoplates. The 1T structure of VTe_2 is further supported by HAADF-STEM and electron energy loss spectrometry (EELS). It can be seen in Figure 2f–i that tellurium atoms (brighter columns) form a hexagonal ring with the weaker contrast vanadium columns in the center of the ring. There are no vanadium vacancies, tellurium vacancies, and other defects in all the examined VTe_2 nanoplates, demonstrating the high quality of the as-grown VTe_2 nanoplates.

To investigate the low-temperature transport properties of the as-grown VTe_2 nanoplates, Hall bar devices were fabricated by standard electron beam lithography (EBL) technique. The inset in Figure 3a shows the optical image of a VTe_2 nanoplate device with the nanoplate thickness of about 87 nm (Figure S10a). Temperature-dependent resistivity (ρ–T) in Figure 3a demonstrates the metallic properties of the VTe_2 nanoplate with a relatively low residual resistivity ratio (RRR = $\rho_{300\ K}/\rho_{2K}$ = 4.58), which is most likely due to the presence of a slight amount of interstitial vanadium ions.[19,30] At high temperatures, the resistivity increases linearly with temperature due to phonon scattering. At low temperatures, the resistivity upturn arises and the resistivity minimum appears at about 8 K (T_m). When applying a strong magnetic field, the resistivity upturn is suppressed as seen in Figure 3b. Usually, resistivity upturn caused by the Kondo effect and weak localization effect disappears under a strong magnetic field, whereas that caused by electron–electron (e–e) interactions cannot be affected by magnetic field.[31−33] To find the origin of the resistivity upturn, magnetoresistance (MR) was measured at different temperatures. Figure 3c shows the transverse MR, which is measured under the magnetic field perpendicular to the electrical current and the *ab* plane of VTe_2 nanoplate. For $T < T_m$, VTe_2 exhibits negative MR (NMR) at low fields. As shown in Figure 3c, the magnetoresistance becomes less steep for high magnetic fields and saturates in fields above about 5 T, exhibiting a crossover from NMR to positive MR. The magnitude of NMR decreases with increasing temperature. When $T > T_m$, the NMR vanishes and positive MR gradually appears. When the magnetic fields are parallel to the electrical current and *ab* plane of VTe_2 nanoplate, the longitudinal MR is still negative at low temperatures (Figure 3d). Figure 3e demonstrates that both the transverse and longitudinal NMR are almost the same and the NMR varies quadratically with increasing magnetic field at low fields. When the contribution of positive quadratic ordinary MR is subtracted in the transverse MR, the transverse and longitudinal NMR are almost exactly the same (Figure S9). However, the positive transverse and longitudinal MR are quite different (Figure 3f). The positive MR is suppressed when the magnetic field is parallel to the electrical current. In other words, the NMR is isotropic and independent of the direction of the magnetic field. However, NMR due to weak localization is anisotropic and vanishes when the magnetic field is parallel to the electrical current.[34] As a consequence, the upturn in resistivity and NMR at low temperatures are attributed to the Kondo effect in which conducting electrons are scattered by localized magnetic moments through isotropic s-d exchange interaction.

The logarithmic upturn in resistivity at low temperatures can be fitted within the framework of the Kondo effect. The resistivity at temperatures ranging from 1.9 to 20 K can be well fitted with the equation[35,36]

$$\rho(T) = \rho_0 + qT^2 + pT^5 + \rho_{K0}\left\{1 - \ln\left(\frac{T}{T_K}\right)\left[ln^2\left(\frac{T}{T_K}\right) + S(S+1)\pi^2\right]^{-1/2}\right\} \quad (1)$$

where the first term is the residual resistivity, the second term represents the Fermi liquid contribution, the third term represents electron–phonon contribution, and the fourth term is the Kondo resistivity, which is described by the Hamann expression, where, ρ_{K0} is temperature-independent resistivity, T_K is the Kondo temperature, and S is the spin of the magnetic impurities. From the fit, $T_K \sim 6.2 \pm 0.45$ K and $S \sim 0.12 \pm 0.04$ are obtained. As shown in Figure 3b, when the magnetic field is applied, broad peaks appear below T_K, and the resistivity curve flattens out with increasing field. This reflects the splitting of the Kondo resonance by an applied magnetic field.[33,37] The temperature dependent resistivity under different magnetic fields are fitted using eq 1 but with a modified Hamann term[37]

$$\rho(H, T) = \rho_{K0}\left\{1 - \ln\left(\frac{T}{T_K}\right)\left[ln^2\left(\frac{T}{T_K}\right) + S(S+1)\pi^2\right]^{-1/2}\right\} \cdot \left\{1 - B^2\left[\frac{g\mu_B H}{k_B(T+T_K)}\right]\right\} \quad (2)$$

where $B(x)$ is a Brillouin function for $S = 1/2$, $B(x) = \frac{2S+1}{2S}\coth\left(\frac{2S+1}{2S}x\right) - \frac{1}{2S}\coth\left(\frac{1}{2S}x\right)$, S is the magnetic impurity spin, g is the Lander factor and $g = 2$,[34,38] μ_B is the Bohr magneton, and k_B is the Boltzmann constant. However, because the temperatures are still around or above T_K, no saturation of resistivity is observed in the absence of magnetic field.

DOI: 10.1021/acs.nanolett.9b03100
Nano Lett. 2019, 19, 8572–8580

In spin-scattering models, the NMR is a function of magnetization of localized magnetic moments. It varies linearly with the square of the effective magnetization $-\frac{\Delta\rho}{\rho} = -\frac{\rho(H)-\rho(0)}{\rho(0)} = \alpha M^2$ and is parabolically dependent on the magnetic field $-\frac{\Delta\rho}{\rho} = S(T)H^2$ at different temperatures.[39,40] The coefficient $S(T)$ is temperature-dependent and proportional to the square of the susceptibility of localized spins $S(T) \propto \chi^2 = f\left(\frac{H}{T}\right)$.[40,41] The value of $S(T)$ can be extracted by fitting the NMR at different temperatures. Figure 4a,b shows the temperature-dependent $S(T)$ and $S(T)^{-1/2}$

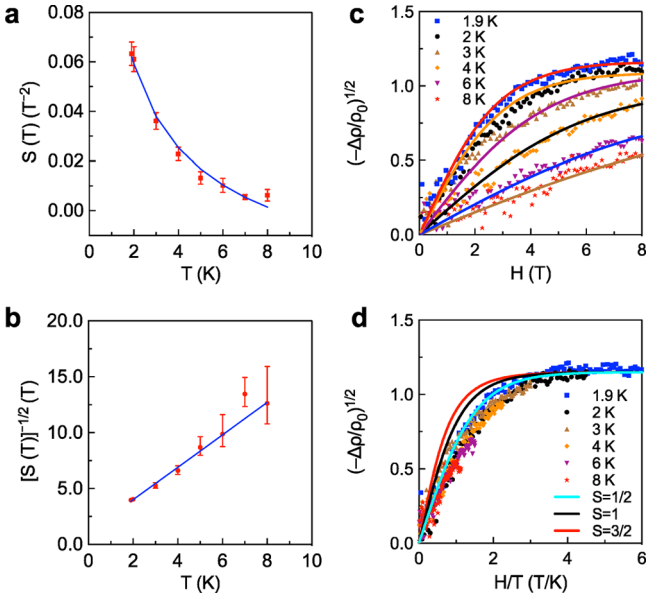

Figure 4. Low-field NMR characteristics at low temperatures. Temperature dependence of the parameter (a) $S(T)$ and (b) $[S(T)]^{-1/2}$ obtained from fits of the low-field NMR at different temperatures. Solid lines in (a,b) are inversely quadratic and linear fit, respectively. $(-\Delta\rho/\rho_0)^{1/2}$ plotted as symbols versus (c) H and (d) H/T respectively. Solid lines in (c) are Brillouin function fits with $S = 1/2$. All the curves at different temperatures are superimposed together in (d) and can be well fitted by a Brillouin function with $S = 1/2$. Quadratic ordinary magnetoresistance obtained by fitting the high field data have been subtracted.

respectively. It can be seen that $S(T)$ is inversely quadratically dependent on temperature or $S(T)^{-1/2}$ is proportional to temperature, $S(T)^{-1/2} \propto (T + T_C)$. This resembles the Curie–Weiss law $\chi = \frac{C}{T+T_C}$, where χ is the magnetic susceptibility, C is the Curie constant, and T_C is the Curie temperature. The fit in Figure 4b corresponds to a value of T_C = 0.76 K. The positive T_C suggests the antiferromagnetic coupling between the localized magnetic moments at $T < T_C$.[40] However, the localized magnetic moments are paramagnetic at $T > T_C$. The magnetic field dependence of square root of NMR is plotted in Figure 4c. It can be well fitted by a Brillouin function with $S = 1/2$. All the curves at different temperatures collapse onto one single scaling curve in Figure 4d. The scaling curve in Figure 4d can only be well fitted by a Brillouin function for $S = 1/2$

$$\left|\frac{\Delta\rho}{\rho_0}\right|^{1/2} = Ng\mu_B SB\left(\frac{g\mu_B SH}{k_B T}\right) \quad (3)$$

The theoretical local magnetic moment of each magnetic scatter center is $g\mu_B\sqrt{S(S+1)} = 1.73\ \mu_B$, assuming quenched orbital moment, which agrees well with the value of intercalated vanadium ions in VX_2 ranging from 1.4 to 2.49 μ_B.[14,17,42]

To reveal the origin of the localized magnetic moments, density functional theory (DFT) calculations were performed. Three types of defect were introduced to understand the stability and magnetic moment that can be brought with defects, that is, tellurium single vacancy (V_{Te}), vanadium single vacancy (V_V), and interstitial vanadium ion at interlayer space (V_{Inter}). The atomic configurations of three types of defect are demonstrated in Figures 5a and S15, and the calculated

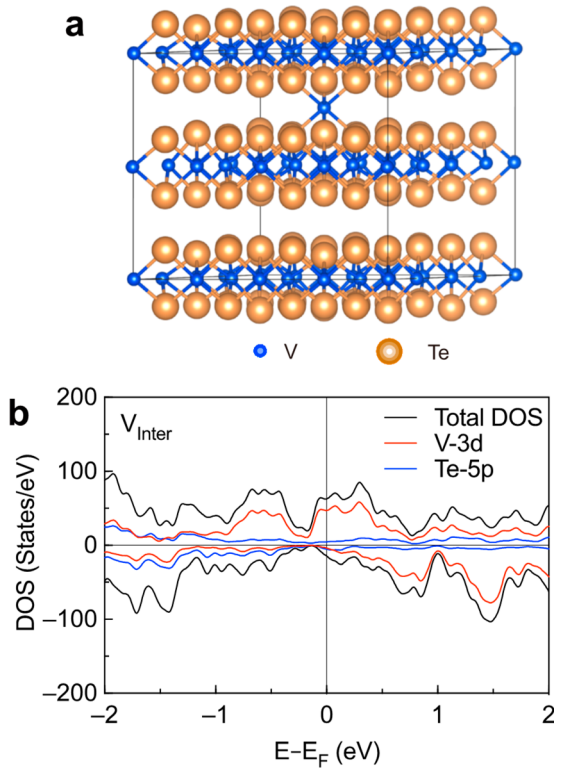

Figure 5. Structure model and DFT simulations of vanadium ions intercalated VTe_2. (a) Atomic structure of vanadium ions intercalated VTe_2. (b) Total, V-3d, and Te-5p orbitals projected DOS of vanadium ions intercalated VTe_2. The Fermi level is set to zero. Positive and negative DOS correspond to spin-up and spin-down components, respectively.

magnetic moments are demonstrated in Table 1. To evaluate the defect formation energy, the chemical potential of vanadium rich (V-rich) and tellurium rich (Te-rich) environment are set as the energy per atom in the corresponding elemental phase of vanadium and tellurium, respectively. It can be inferred from Table 1 that in a V-rich environment, the V_{Inter} defect has the lowest formation energy, which indicates that when vanadium source is excessive, or locally excessive, the V_{Inter} defect is mostly likely to form thermodynamically. This agrees well with the fact that the V–X (X = S, Se, Te) systems tend to form self-intercalated compounds.[43] Furthermore,

DOI: 10.1021/acs.nanolett.9b03100
Nano Lett. 2019, 19, 8572−8580

Table 1. Calculated Formation Energy and Magnetic Moment for Different Defects

	formation energy (eV)			
configuration	V-rich	Te-rich	magnetic moment (μ_B)	moment difference (μ_B)
perfect VTe_2			1.30	
V_{Te}	−0.88	−0.40	0.21	−1.09
V_V	0.25	−0.72	1.30	0
V_{Inter}	−1.03	−0.05	2.03	0.73

V_{Inter} leads to the enhancement of magnetic moment of 0.73 μ_B, which mainly provides the local moment leading to the Kondo effect. The projected density of states (PDOS) of the defect-free VTe_2 and the three defect complexes are calculated and demonstrated in Figures 5b and S15. The defect-free VTe_2 is spin polarized and ferromagnetic due to the unpaired $3d^1$ electron of each vanadium ion in VTe_2, whereas the contribution of the tellurium anion is small (Figure S15b). It is consistent with the calculated magnetic properties of bulk VS_2 and VSe_2.[9,44,45] However, a previous report indicates that the ferromagnetism is suppressed by the charge-density-wave state, and no intrinsic ferromagnetic ordering is observed in VTe_2, even in the monolayer limit.[46] Although we do not have direct evidence on the presence of charge-density-wave state in our VTe_2 nanoplates, to clarify the competition between the ferromagnetism and charge-density-wave in VTe_2 further studies are needed. When defects are introduced, the spin polarization changes with respect to the defect configurations. For vanadium and tellurium vacancy, the spin polarization weakens (Figure S15d,f). However, for vanadium ions intercalated VTe_2, the spin polarization is enhanced and is the largest among all the samples. As shown in Figure 5b, the DOS of vanadium ions intercalated VTe_2 demonstrates a significant asymmetry between the spin-up and spin-down states. As a consequence, we believe that the localized magnetic moments mainly originate from the interstitial vanadium ions. The interstitial V ions may come from the nonuniformly distributed vanadium precursor or fluctuations in growth parameters such as growth temperature and carrier gas, because of their low formation energy. It is also supported by the fact that interstitial vanadium ions provide localized magnetic moments in V_5S_8 and VSe_2.[16,42] We tried to find the interstitial vanadium ions through HAADF-STEM image (Figure S7), unfortunately, we did not find a clearly resolved image to show the existence of the vanadium interstitials, which is probably due to the fluctuation of distributed V interstitials and the interstitials are in very small portion in the VTe_2 nanoplates.

No change of the resistivity upturn and NMR in the VTe_2 devices after stored for half a year suggests that the localized magnetic moments are not introduced by vanadium and tellurium vacancies (Figure S10). The degradation of VTe_2 during storage, which may introduce vanadium and tellurium vacancies, is confirmed by XPS (Figure S14). No anomalous Hall effect is observed in all the VTe_2 nanoplates with various thicknesses in the whole range of temperature (Figure S12), which indicates that no intrinsic long-range ferromagnetic order occurs in the individual multilayer VTe_2 nanoplates. Magnetization measurement also supports the transport results. As-grown VTe_2 nanoplates exhibit soft ferromagnetic behavior at low temperatures, whereas at high temperatures, superparamagnetism or spin-glass-like state are observed (Figure S16), which probably originates from the inhomogeneous interstitial vanadium ions or vanadium ion clusters. The absence of ferromagnetism in multilayer VTe_2 nanoplates, particularly at room temperature, would be due to the large thickness or the existence of competing charge-density-wave ground state[11,46−51] or spin frustration analogous to VSe_2.[52]

The degradation will be exacerbated in ultrathin VTe_2 nanoplates and the e−e interactions (Altshuler−Aronov effect) will be enhanced. Meanwhile, previous studies on the thickness-dependent Kondo effect have shown that the Kondo effect is partially suppressed with decreasing film thickness.[53] Consequently, a more pronounced Kondo effect, that is, large slope of the logarithmic temperature-dependent Kondo resistivity, will be shown in thicker VTe_2 nanoplates. Low-temperature transport studies of ultrathin VTe_2 devices show that e−e interactions in thinner (34 nm) VTe_2 nanoplates emerges and leads to a resistivity upturn similar to the Kondo effect (Figure S13).[32,54] In contrast to the Kondo effect, the upturn in resistivity due to e−e interactions cannot be suppressed by strong magnetic field. Furthermore, MR due to e−e interactions is positive in ultrathin VTe_2 nanoplates as shown in Figure S13b−f, whereas the Kondo effect leads to NMR at low magnetic fields and low temperatures. As a consequence, in ultrathin VTe_2 nanoplates, e−e interactions compete with the Kondo effect, which will make the system complicated. In order to obtain a relatively pure Kondo effect, multilayer thicker VTe_2 nanoplates are much more preferable. Surface state also rules out multilayer thicker VTe_2 nanoplates. The intercalated vanadium ions in VTe_2 nanoplates are in trace amounts and randomly distributed, so they do not affect the crystal structure of VTe_2; there are no Kondo lattice forms in this system.[55] When more vanadium ions are intercalated in the van der Waals gaps of VTe_2, Kondo lattice or even magnetic ordering will be obtained.[17,18,42]

In conclusion, 1T phase multilayer VTe_2 nanoplates have been successfully grown by atmospheric pressure CVD using a sublimed salt as a growth promoter. The high-quality VTe_2 nanoplates are characterized by OM, AFM, XRD, XPS, SEM, and TEM. Low-temperature transport demonstrates the presence of localized magnetic moments and the Kondo effect in the individual multilayer metallic VTe_2 nanoplates, that is, logarithmic temperature dependence of resistivity upturn accompanied with NMR at low magnetic fields at temperatures below the resistivity minimum. The resistivity upturn can be well fitted with the Hamann expression by which the Kondo temperature T_K is obtained about 6.2 K. The NMR is independent of the relative orientation of magnetic field and electrical current, which suggests that conduction electrons are scattered by localized magnetic moments through isotropic s-d exchange interaction. DFT calculations demonstrate that interstitial vanadium ions are the main origin of the localized magnetic moments. The Kondo effect in ultrathin VTe_2 nanoplates is suppressed by the enhanced e−e interactions or less interstitial vanadium ions. No signature of intrinsic long-range ferromagnetic order is observed in the multilayer VTe_2 nanoplates. Further studies still need to be carried out to study the formation, valence state, and concentration of the interstitial vanadium ions in the VTe_2 nanoplates. Controllable introducing interstitial vanadium ions into VX_2 and other 2D TMDs will enrich the material pool for spintronic applications and fundamental studies of magnetism at the 2D limit. The results presented here will lead to the study of the Kondo

DOI: 10.1021/acs.nanolett.9b03100
Nano Lett. 2019, 19, 8572−8580

effect, strong correlation, or many-body physics in 2D TMDs and also shed light on the magnetic properties in VX_2.

Methods. *CVD Growth of VTe_2.* VTe_2 was grown in a two-zone furnace by atmospheric pressure CVD. About 1 g of tellurium lump (Alfa Aesar, 99.999+%) was used as the tellurium source and placed in a quartz boat that was loaded upstream in the first zone of a two-zone furnace. 10 milligrams of the well-ground mixture of vanadium (V) oxide (V_2O_5, Alfa Aesar, 99.99%) and ammonium chloride (NH_4Cl, Alfa Aesar, 99.999%) with a weight ratio of 1:20 was used as the vanadium source and placed in another quartz boat that was loaded downstream in the second zone. The substrate (SiO_2/Si or mica) was placed vertically about 1 cm downward from the vanadium source. Before ramping up the temperature, the furnace was first evacuated for 5 min without carrier gas, and then evacuated for another 5 min with 300 sscm hydrogen/argon (1:9, v/v). At last, the evacuation was stopped and the hydrogen/argon gas was filled in the furnace to atmospheric pressure. The temperature of tellurium and vanadium source was set to 750 °C for 15 min and kept for 20 min. Then it was rapidly cooled down to room temperature. Hydrogen/argon (300 sccm) was used as the carrier gas during the whole growth process.

Characterization of VTe_2. The as-grown VTe_2 nanoplates were characterized by optical microscope (Olympus BX51-SC30), scanning electron microscope (SEM, Hitachi S-4800, acceleration voltage of 10 kV, EDS 15 kV), atomic force microscope (AFM, Digital Instruments Nanoscope IIIa) operated in tapping mode, transmission electron microscope (TEM, EM-2100F, JEOL, operating at 200 kV and equipped with an EDS system), X-ray photoelectron spectroscopy (XPS, ESCALAB 250Xi spectrometer, Thermo Fisher Scientific), and X-ray diffraction (XRD, Bruker D2 phaser PHASER diffractometer with Cu−Kα radiation, λ = 1.54184 Å) operating at 30 kV and 10 mA at room temperature. Aberration-corrected scanning transmission electron microscopy (STEM) imaging and electron energy loss spectroscopy (EELS) mapping were performed using a Nion HERMES-100, operated at 100 kV. Because of partial overlapping of the V L-edge (513 eV) and Te M-edge (572 eV), the multiple linear least-squares (MLLS) fitting method was used to extract the chemical map from as-acquired spectrum imaging.

Device Fabrication and Transport Measurement. The as-grown VTe_2 nanoplates were transferred onto a precleaned SiO_2/Si substrate using the face-to-face transfer method.[29] A 300 nm thick poly(methyl methacrylate) (PMMA, molecular weights 950 K, 5% dilution of PMMA in anisole) film was spin-coated on it at a speed of 4000 rpm for 60 s. In order to avoid degradation of the VTe_2 nanoplate during the conventional high-temperature baking, it was baked at 60 °C in a vacuum oven overnight. Hall bar devices were fabricated by a standard electron beam lithography technique (Raith 150), followed by electron-beam evaporation of 5/100 nm Ti/Au metal stacks as contact electrodes. All transport measurements were performed in a physical property measurement system (PPMS, Quantum Design Inc.) using the resistivity option with alternating current (ac) drive mode. While performing the $\rho-T$ measurement, the cooling/warming rate was 2 K/min. In order to measure the longitudinal MR, a homemade rotator rod was used. The direct current (dc) magnetization measurements were carried out with a Quantum Design Magnetic Property Measurement System MPMS SQUID VSM. The VTe_2 nanoplates were carefully transferred onto Kapton tape for magnetization measurement to exclude any signals from the substrate.

Density Functional Theory (DFT) Calculations. All DFT calculations were performed with the Vienna ab initio simulation package (VASP) using the Perdew−Burke−Ernzerhof (PBE) functional and projector augmented-wave (PAW) method.[56−58] A supercell of 4 × 4 × 2 was constructed for modeling different types of defects in which the interaction between defect and its image was larger than 1.3 nm. The dispersive van der Waals interactions between different VTe_2 layers were considered using the DFT-D2 method of Grimme.[59,60] In each calculation, an energy cutoff of 520 eV was adopted whereas a higher cutoff will have an energy difference of less than 0.01 eV. When performing the structure optimizations, the system was regarded as converged when the force per atom was less than 0.01 eV/Å.

■ ASSOCIATED CONTENT

Supporting Information

The Supporting Information is available free of charge at https://pubs.acs.org/doi/10.1021/acs.nanolett.9b03100.

Additional figures regarding CVD growth, OM, SEM, SAED, TEM, transport, XPS, and DFT calculations of VTe_2 (PDF)

■ AUTHOR INFORMATION

Corresponding Author

*E-mail: lhbao@iphy.ac.cn.

ORCID

Hongtao Liu: 0000-0003-0500-7204
Lihong Bao: 0000-0002-2942-892X
Hong-Jun Gao: 0000-0002-6766-0623

Author Contributions

#H.L. and Y.X. contributed equally.

Notes

The authors declare no competing financial interest.

■ ACKNOWLEDGMENTS

This work was supported by National Key Research & Development Projects of China (Grants 2016YFA0202300, 2018FYA0305800), National Natural Science Foundation of China (Grants 61674170, 61888102, 61904113), Strategic Priority Research Program of Chinese Academy of Sciences (CAS, Grants XDB30000000, XDB28000000), Youth Innovation Promotion Association of CAS (20150005), and Science and Technology Innovation Commission of Shenzhen (JCYJ20180305125616770). The authors would like to thank Prof. Haifang Yang, Prof. Junjie Li, and Prof. Changzhi Gu in Laboratory of Microfabrication, Institute of Physics, CAS for the support of device fabrication, and the STEM assistance from the Electron Microscopy Center of the Shenzhen University.

■ REFERENCES

(1) Huang, B.; Clark, G.; Navarro-Moratalla, E.; Klein, D. R.; Cheng, R.; Seyler, K. L.; Zhong, D.; Schmidgall, E.; McGuire, M. A.; Cobden, D. H.; Yao, W.; Xiao, D.; Jarillo-Herrero, P.; Xu, X. Layer-Dependent Ferromagnetism in a van Der Waals Crystal down to the Monolayer Limit. *Nature* **2017**, *546* (7657), 270−273.

(2) Gong, C.; Li, L.; Li, Z.; Ji, H.; Stern, A.; Xia, Y.; Cao, T.; Bao, W.; Wang, C.; Wang, Y.; Qiu, Z. Q.; Cava, R. J.; Louie, S. G.; Xia, J.;

DOI: 10.1021/acs.nanolett.9b03100
Nano Lett. 2019, 19, 8572−8580

Zhang, X. Discovery of Intrinsic Ferromagnetism in Two-Dimensional van Der Waals Crystals. *Nature* **2017**, *546* (7657), 265−269.
(3) Song, T.; Cai, X.; Tu, M. W.-Y.; Zhang, X.; Huang, B.; Wilson, N. P.; Seyler, K. L.; Zhu, L.; Taniguchi, T.; Watanabe, K.; McGuire, M. A.; Cobden, D. H.; Xiao, D.; Yao, W.; Xu, X. Giant Tunneling Magnetoresistance in Spin-Filter van der Waals Heterostructures. *Science* **2018**, *360* (6394), 1214−1218.
(4) Klein, D. R.; MacNeill, D.; Lado, J. L.; Soriano, D.; Navarro-Moratalla, E.; Watanabe, K.; Taniguchi, T.; Manni, S.; Canfield, P.; Fernandez-Rossier, J.; Jarillo-Herrero, P. Probing Magnetism in 2D van der Waals Crystalline Insulators via Electron Tunneling. *Science* **2018**, *360* (6394), 1218−1222.
(5) Gong, C.; Zhang, X. Two-Dimensional Magnetic Crystals and Emergent Heterostructure Devices. *Science* **2019**, *363* (6428), eaav4450.
(6) Ma, Y.; Dai, Y.; Guo, M.; Niu, C.; Zhu, Y.; Huang, B. Evidence of the Existence of Magnetism in Pristine VX_2 Monolayers (X = S, Se) and Their Strain-Induced Tunable Magnetic Properties. *ACS Nano* **2012**, *6* (2), 1695−1701.
(7) Zhang, H.; Liu, L.-M.; Lau, W.-M. Dimension-Dependent Phase Transition and Magnetic Properties of VS_2. *J. Mater. Chem. A* **2013**, *1* (36), 10821−10828.
(8) Pan, H. Electronic and Magnetic Properties of Vanadium Dichalcogenides Monolayers Tuned by Hydrogenation. *J. Phys. Chem. C* **2014**, *118* (24), 13248−13253.
(9) Wasey, A. H. M. A.; Chakrabarty, S.; Das, G. P. Quantum Size Effects in Layered VX_2 (X = S, Se) Materials: Manifestation of Metal to Semimetal or Semiconductor Transition. *J. Appl. Phys.* **2015**, *117* (6), 064313.
(10) Fuh, H.-R.; Chang, C.-R.; Wang, Y.-K.; Evans, R. F. L.; Chantrell, R. W.; Jeng, H.-T. Newtype Single-Layer Magnetic Semiconductor in Transition-Metal Dichalcogenides VX_2 (X = S, Se and Te). *Sci. Rep.* **2016**, *6*, 32625.
(11) Bonilla, M.; Kolekar, S.; Ma, Y.; Diaz, H. C.; Kalappattil, V.; Das, R.; Eggers, T.; Gutierrez, H. R.; Manh-Huong, P.; Batzill, M. Strong Room-Temperature Ferromagnetism in VSe_2 Monolayers on van Der Waals Substrates. *Nat. Nanotechnol.* **2018**, *13* (4), 289−293.
(12) Vanbruggen, C. F.; Haas, C. Magnetic Susceptibility and Electrical Properties of VSe_2 Single Crystals. *Solid State Commun.* **1976**, *20* (3), 251−254.
(13) Thompson, A. H.; Silbernagel, B. G. Magnetic Properties of VSe_2: Inferences From the Study of Metal-Rich $V_{1+\delta}Se_2$ Compounds. *J. Appl. Phys.* **1978**, *49* (3), 1477−1479.
(14) Disalvo, F. J.; Waszczak, J. V. Magnetic Studies of VSe_2. *Phys. Rev. B: Condens. Matter Mater. Phys.* **1981**, *23* (2), 457−461.
(15) Mutka, H.; Molinie, P. Irradiation-Induced Defects in Layered Dichalcogenides: the Case of VSe_2. *J. Phys. C: Solid State Phys.* **1982**, *15* (31), 6305−6319.
(16) Barua, S.; Hatnean, M. C.; Lees, M. R.; Balakrishnan, G. Signatures of the Kondo Effect in VSe_2. *Sci. Rep.* **2017**, *7*, 10964.
(17) Hardy, W. J.; Yuan, J.; Guo, H.; Zhou, P.; Lou, J.; Natelson, D. Thickness-Dependent and Magnetic-Field-Driven Suppression of Antiferromagnetic Order in Thin V_5S_8 Single Crystals. *ACS Nano* **2016**, *10* (6), 5941−5946.
(18) Niu, J.; Yan, B.; Ji, Q.; Liu, Z.; Li, M.; Gao, P.; Zhang, Y.; Yu, D.; Wu, X. Anomalous Hall Effect and Magnetic Orderings in Nanothick V_5S_8. *Phys. Rev. B: Condens. Matter Mater. Phys.* **2017**, *96* (7), 075402.
(19) Ding, X. Transport Research on $K_xFe_{2-y}Se_2$ and VTe_2 Single Crystals. 2015, Ph.D. Thesis, Nanjing University.
(20) Hewson, A. C. *The Kondo Problem to Heavy Fermions*; Cambridge University Press: Cambridge, 1993.
(21) Kondo, J. Resistance Minimum in Dilute Magnetic Alloys. *Prog. Theor. Phys.* **1964**, *32* (1), 37−49.
(22) Zhang, S.; Ogale, S. B.; Yu, W.; Gao, X.; Liu, T.; Ghosh, S.; Das, G. P.; Wee, A. T. S.; Greene, R. L.; Venkatesan, T. Electronic Manifestation of Cation-Vacancy-Induced Magnetic Moments in a Transparent Oxide Semiconductor: Anatase Nb:TiO_2. *Adv. Mater.* **2009**, *21* (22), 2282−2287.
(23) Chen, J.-H.; Li, L.; Cullen, W. G.; Williams, E. D.; Fuhrer, M. S. Tunable Kondo Effect in Graphene with Defects. *Nat. Phys.* **2011**, *7* (7), 535−538.
(24) Lee, M.; Williams, J. R.; Zhang, S.; Frisbie, C. D.; Goldhaber-Gordon, D. Electrolyte Gate-Controlled Kondo Effect in $SrTiO_3$. *Phys. Rev. Lett.* **2011**, *107* (25), 256601.
(25) Cha, J. J.; Claassen, M.; Kong, D.; Hong, S. S.; Koski, K. J.; Qi, X.-L.; Cui, Y. Effects of Magnetic Doping on Weak Antilocalization in Narrow Bi_2Se_3 Nanoribbons. *Nano Lett.* **2012**, *12* (8), 4355−4359.
(26) Li, Y.; Deng, R.; Lin, W.; Tian, Y.; Peng, H.; Yi, J.; Yao, B.; Wu, T. Electrostatic Tuning of Kondo Effect in a Rare-Earth-Doped Wide-Band-Gap Oxide. *Phys. Rev. B: Condens. Matter Mater. Phys.* **2013**, *87* (15), 155151.
(27) Ren, J.; Guo, H.; Pan, J.; Zhang, Y. Y.; Wu, X.; Luo, H.-G.; Du, S.; Pantelides, S. T.; Gao, H.-J. Kondo Effect of Cobalt Adatoms on a Graphene Monolayer Controlled by Substrate-Induced Ripples. *Nano Lett.* **2014**, *14* (7), 4011−4015.
(28) Li, J.; Zhao, B.; Chen, P.; Wu, R.; Li, B.; Xia, Q.; Guo, G.; Luo, J.; Zang, K.; Zhang, Z.; Ma, H.; Sun, G.; Duan, X.; Duan, X. Synthesis of Ultrathin Metallic MTe_2 (M = V, Nb, Ta) Single-Crystalline Nanoplates. *Adv. Mater.* **2018**, *30* (36), 1801043.
(29) Liu, H.; Bao, L.; Zhou, Z.; Che, B.; Zhang, R.; Bian, C.; Ma, R.; Wu, L.; Yang, H.; Li, J.; Gu, C.; Shen, C.-M.; Du, S.; Gao, H.-J. Quasi-2D Transport and Weak Antilocalization Effect in Few-layered VSe_2. *Nano Lett.* **2019**, *19* (7), 4551−4559.
(30) Kamitani, M.; Sonobe, T. Single Crystal Growth of Ti Doped VTe_2 and the Elucidation of the Electronic Sructure by ARPES. http://www.ap.t.u-tokyo.ac.jp/merit/en/training/pdf/report/jihatsu_kamitani-sonobe_eng.pdf 2015 (accessed on May 7, 2015).
(31) Bergmann, G. Weak Localization in Thin Films: A Time-of-Flight Experiment with Conduction Electrons. *Phys. Rep.* **1984**, *107* (1), 1−58.
(32) Lee, P. A.; Ramakrishnan, T. V. Disordered Electronic Systems. *Rev. Mod. Phys.* **1985**, *57* (2), 287−337.
(33) Costi, T. A. Kondo Effect in a Magnetic Field and the Magnetoresistivity of Kondo Alloys. *Phys. Rev. Lett.* **2000**, *85* (7), 1504−1507.
(34) Cao, Q.; Yun, F. F.; Sang, L.; Xiang, F.; Liu, G.; Wang, X. Defect Introduced Paramagnetism and Weak Localization in Two-Dimensional Metal VSe_2. *Nanotechnology* **2017**, *28* (47), 475703.
(35) Hamann, D. R. New Solution for Exchange Scattering in Dilute Alloys. *Phys. Rev.* **1967**, *158* (3), 570−580.
(36) Brinkman, A.; Huijben, M.; Van Zalk, M.; Huijben, J.; Zeitler, U.; Maan, J. C.; Van der Wiel, W. G.; Rijnders, G.; Blank, D. H. A.; Hilgenkamp, H. Magnetic Effects at the Interface Between Non-Magnetic Oxides. *Nat. Mater.* **2007**, *6* (7), 493−496.
(37) Felsch, W.; Winzer, K. Magnetoresistivity of (La, Ce)Al_2 Alloys. *Solid State Commun.* **1973**, *13* (5), 569−573.
(38) Kondo, S.; Johnston, D. C.; Miller, L. L. Synthesis, characterization, and magnetic susceptibility of the heavy-fermion transition-metal oxide LiV_2O_4. *Phys. Rev. B: Condens. Matter Mater. Phys.* **1999**, *59* (4), 2609−2626.
(39) Yosida, K. Anomalous Electrical Resistivity and Magnetoresistance Due to an s-d Interaction in Cu-Mn Alloys. *Phys. Rev.* **1957**, *107* (2), 396−403.
(40) Katayama, Y.; Tanaka, S. Resistance Anomaly and Negative Magnetoresistance in n-Type InSb at Very Low Temperatures. *Phys. Rev.* **1967**, *153* (3), 873−882.
(41) Toyozawa, Y. Theory of Localized Spins and Negative Magnetoresistance in the Metallic Impurity Conduction. *J. Phys. Soc. Jpn.* **1962**, *17* (6), 986−1004.
(42) Niu, J.; Li, Z.; Yang, S.; Zhang, W.; Yan, D.; Chen, S.; Zhang, Z.; Zhang, Y.; Ren, X.; Gao, P.; Shi, Y.; Yu, D.; Wu, X. V_5S_8: A Kondo Lattice Based on Intercalation of van Der Waals Layered Transition Metal Dichalcogenide. **2018**, arXiv:1809.04213.
(43) Lieth, R. M. A. *Preparation and Crystal Growth of Materials with Layered Structures*, 1st ed.; Springer Netherlands, 1977; Vol. *1*, pp 178−180.

DOI: 10.1021/acs.nanolett.9b03100
Nano Lett. 2019, 19, 8572−8580

(44) Li, F.; Tu, K.; Chen, Z. Versatile Electronic Properties of VSe_2 Bulk, Few-Layers, Monolayer, Nanoribbons, and Nanotubes: A Computational Exploration. *J. Phys. Chem. C* **2014**, *118* (36), 21264−21274.
(45) Xu, K.; Chen, P.; Li, X.; Wu, C.; Guo, Y.; Zhao, J.; Wu, X.; Xie, Y. Ultrathin Nanosheets of Vanadium Diselenide: A Metallic Two-Dimensional Material with Ferromagnetic Charge-Density-Wave Behavior. *Angew. Chem., Int. Ed.* **2013**, *52* (40), 10477−10481.
(46) Coelho, P. M.; Lasek, K.; Cong, K. N.; Li, J. F.; Niu, W.; Liu, W. Q.; Oleynik, I. I.; Batzill, M. Monolayer Modification of VTe_2 and Its Charge Density Wave. *J. Phys. Chem. Lett.* **2019**, *10* (17), 4987−4993.
(47) Sugawara, K.; Nakata, Y.; Fujii, K.; Nakayama, K.; Souma, S.; Takahashi, T.; Sato, T. Monolayer VTe_2: Incommensurate Fermi surface nesting and suppression of charge density waves. *Phys. Rev. B: Condens. Matter Mater. Phys.* **2019**, *99* (24), 241404.
(48) Coelho, P. M.; Kien Nguyen, C.; Bonilla, M.; Kolekar, S.; Manh-Huong, P.; Avila, J.; Asensio, M. C.; Oleynik, I. I.; Batzill, M. Charge Density Wave State Suppresses Ferromagnetic Ordering in VSe_2 Monolayers. *J. Phys. Chem. C* **2019**, *123* (22), 14089−14096.
(49) Wang, Y.; Ren, J.; Li, J.; Wang, Y.; Peng, H.; Yu, P.; Duan, W.; Zhou, S. Evidence of Charge Density Wave with Anisotropic Gap in Monolayer VTe_2 Film. **2019**, arXiv:1909.13446 (accessed on May 31, 2019).
(50) Wong, P. K. J.; Zhang, W.; Zhou, J.; Bussolotti, F.; Yin, X.; Zhang, L.; NDiaye, A. T.; Morton, S. A.; Chen, W.; Goh, E. J. K.; de Jong, M. P.; Feng, Y. P.; Wee, A. T. S. Evidence for Metallic 1T Phase, $3d^1$ Electronic Configuration and Charge Density Wave Order in Molecular-Beam Epitaxy Grown Monolayer VTe_2 . *ACS NANO* [Online early access]. DOI: 10.1021/acsnano.9b05349. Published Online: Nov 6, **2019**, https://pubs.acs.org/doi/10.1021/acsnano.9b05349.
(51) Miao, G.; Xue, S.; Li, B.; Lin, Z.; Liu, B.; Zhu, X.; Wang, W.; Guo, J. Real-Space Investigation of the Charge Density Wave in VTe_2 Monolayer with Rotational and Mirror Symmetries Broken. **2019**, arXiv:1908.00714 (accessed on August 2, 2019).
(52) Wong, P. K. J.; Zhang, W.; Bussolotti, F.; Yin, X.; Herng, T. S.; Zhang, L.; Huang, Y. L.; Vinai, G.; Krishnamurthi, S.; Bukhvalov, D. W.; Zheng, Y. J.; Chua, R.; N'Diaye, A. T.; Morton, S. A.; Yang, C.-Y.; Yang, K.-H. O.; Torelli, P.; Chen, W.; Goh, K. E. J.; Ding, J.; Lin, M.-T.; Brocks, G.; de Jong, M. P.; Neto, A. H. C.; Wee, A. T. S. Evidence of Spin Frustration in a Vanadium Diselenide Monolayer Magnet. *Adv. Mater.* **2019**, *31* (23), 1901185.
(53) Apostolopoulos, G.; Papastaikoudis, C. The Influence of Thickness on the Kondo Effect in Cu(Fe) Thin Films. *Solid State Commun.* **1996**, *99* (4), 277−281.
(54) Altshuler, B. L.; Aronov, A. G. Electron−Electron Interaction In Disordered Conductors. In *Modern Problems in Condensed Matter Sciences*; Efros, A. L., Pollak, M., Eds.; Elsevier, 1985; Vol. *10*, Chapter 1, pp 1−153.
(55) Doniach, S. The Kondo Lattice and Weak Antiferromagnetism. *Physica B+C* **1977**, *91*, 231−234.
(56) Hohenberg, P.; Kohn, W. Inhomogeneous Electron Gas. *Phys. Rev.* **1964**, *136* (3B), B864−B871.
(57) Kohn, W.; Sham, L. J. Self-Consistent Equations Including Exchange and Correlation Effects. *Phys. Rev.* **1965**, *140* (4A), A1133−A1138.
(58) Blochl, P. E. Projector Augmented-Wave Method. *Phys. Rev. B: Condens. Matter Mater. Phys.* **1994**, *50* (24), 17953−17979.
(59) Grimme, S. Semiempirical GGA-Type Density Functional Constructed with a Long-Range Dispersion Correction. *J. Comput. Chem.* **2006**, *27* (15), 1787−1799.
(60) Grimme, S.; Antony, J.; Ehrlich, S.; Krieg, H. A Consistent and Accurate Ab Initio Parametrization of Density Functional Dispersion Correction (DFT-D) for the 94 Elements H-Pu. *J. Chem. Phys.* **2010**, *132* (15), 154104.

DOI: 10.1021/acs.nanolett.9b03100
Nano Lett. 2019, 19, 8572−8580